

EXTENDED STRUCTURE AND FATE OF THE NUCLEUS IN HENIZE 2-10

DIEU D. NGUYEN¹, ANIL C. SETH¹, AMY E. REINES², MARK DEN BROK¹, DAVID SAND³, AND BRIAN MCLEOD⁴*Draft version August 25, 2014*

ABSTRACT

We investigate the structure and nuclear region of the black hole (BH) hosting galaxy Henize 2-10. Surface brightness (SB) profiles are analyzed using Magellan/Megacam g - and r -band images. Excluding the central starburst, we find a best-fit two component Sérsic profile with $n_{\text{in}} \sim 0.6$, $r_{\text{eff, in}} \sim 260$ pc, and $n_{\text{out}} \sim 1.8$, $r_{\text{eff, out}} \sim 1$ kpc. Integrating out to our outer most data point ($100'' \sim 4.3$ kpc), we calculate $M_g = -19.2$ and $M_r = -19.8$. The corresponding enclosed stellar mass is $M_\star \sim (10 \pm 3) \times 10^9 M_\odot$, $\sim 3\times$ larger than previous estimates. Apart from the central $\lesssim 500$ pc, with blue colors and an irregular morphology, the galaxy appears to be an early-type system. The outer color is quite red, $(g-r)_0 = 0.75$, suggesting a dominant old population. We study the nuclear region of the galaxy using archival Gemini/NIFS K -band adaptive optics spectroscopy and *Hubble Space Telescope* imaging. We place an upper limit on the BH mass of $\sim 10^7 M_\odot$ from the NIFS data, consistent with that from the M_{BH} -radio-X-ray fundamental plane. No coronal lines are seen, but a Br γ source is located at the position of the BH with a luminosity consistent with the X-ray emission. The starburst at the center of Henize 2-10 has led to the formation of several super star clusters, which are within ~ 100 pc of the BH. We examine the fate of the nucleus by estimating the dynamical masses and dynamical friction timescales of the clusters. The most massive clusters ($\sim 10^6 M_\odot$) have $\tau_{\text{dyn}} \lesssim 200$ Myr, and thus Henize 2-10 may represent a rare snapshot of nuclear star cluster formation around a pre-existing massive BH.

Subject headings: methods: data analysis—techniques: spectroscopic—surveys

1. INTRODUCTION

The nuclei of galaxies are typically inhabited by both massive black holes (BHs) and nuclear star clusters (NSCs). BHs have been found to be ubiquitous in galaxies more massive than the Milky Way, but at lower masses the picture is less clear. BHs have been found in galaxies up to 100 times lower mass than the Milky Way (Verolme et al. 2002; Barth 2004; Greene et al. 2008; Seth et al. 2010; Reines et al. 2013, 2014), but the occupation fraction of BHs in these galaxies remains uncertain (Greene 2012; Miller et al. 2014). NSCs are very common in fainter galaxies; about 75% of galaxies with stellar masses between 5×10^8 and $10^{11} M_\odot$ have NSCs (Böker et al. 2002; Côté et al. 2006; Seth et al. 2008). The formation and evolution of BHs and NSCs is not well understood. BHs are thought to originally form in the early universe from direct collapse or the remnants of Population III stars, and then grow through merger-induced or secular gas accretion, or through accretion of stellar material (Volonteri 2010). An indirect way of probing the formation of these ob-

jects is by examining how their mass scales with the properties of their host galaxies. These scaling relationships have been studied for both BHs and NSCs, and their masses have been found to correlate strongly (Ferrarese et al. 2006a; Graham 2012; Leigh et al. 2012). Initially, Ferrarese et al. (2006a) and Wehner & Harris (2006) found that NSCs and BHs scale similarly with the mass of their host galaxies. However, this claim has been disputed by more recent work (Scott et al. 2013).

In the context of BH and NSC formation, Henize 2-10 is a particularly interesting object. It is undergoing a major nuclear starburst with a star formation rate $1.9 M_\odot \text{ yr}^{-1}$ (Méndez et al. 1999; Engelbracht et al. 2005; Calzetti et al. 2007). A vast majority of this star formation is taking place in a very small region around the center of the galaxy with a diameter of 120 pc ($3''$). There are many super star clusters (SSCs) $> 10^5 M_\odot$ forming in this nuclear starburst, and these have been age-dated to be < 5 Myr (Chandar et al. 2003). A luminous nuclear X-ray point source was found by Ott et al. (2005a,b). Kobulnicky & Martin (2010) suggested it may be an intermediate-mass BH or ultraluminous X-ray source. Stronger evidence for the existence of an accreting massive BH was recently found by Reines et al. (2011), who showed that the X-ray source was coincident with a radio source. The luminosities of this source are consistent with a $\sim 10^6 M_\odot$ BH lying on the fundamental plane (Merloni et al. 2003). Reines et al. (2011) find that alternative explanations for this source are not plausible, and conclude that there is likely an accreting BH. The source is not coincident with any of the known SSCs and parsec-scale non-thermal radio emission is detected from the source with very long baseline interferometry observations (Reines & Deller 2012).

¹ Department of Physics and Astronomy, University of Utah, 115 South 1400 East, Salt Lake City, UT 84112, USA
dieu.nguyen@utah.edu
aseth@astro.utah.edu
denbrok@physics.utah.edu

² National Radio Astronomy Observatory, Charlottesville, VA 22903, USA, Einstein Fellow
areines@nrao.edu

³ Department of Physics, Texas Tech University, 2500 Broadway St, Lubbock, TX 79409, USA
david.sand@ttu.edu

⁴ Harvard-Smithsonian Center for Astrophysics, Harvard University, 60 Garden St, Cambridge, MA 02138, USA
bmcleod@cfa.harvard.edu

In this paper, we focus on three aspects of what this interesting galaxy can tell us about BH and NSC formation. First, we examine the extended structure and stellar mass of the galaxy and place it in a broader context. Next, we examine the kinematics of the nuclear region, and use this information to look at whether an NSC can form from the existing population of SSCs found in the nucleus. Finally, we examine the infrared spectra at the location of the putative BH for any signs of BH accretion visible in the NIR.

Henize 2-10 is a blue compact dwarf or Wolf-Rayet galaxy, with an absolute B -band magnitude of -19.07 ($6.5 \times 10^9 L_\odot$) (Micheva et al. 2013). Due to its low Galactic latitude ($b = 8.6^\circ$) and significant foreground contamination, Henize 2-10's larger scale structure has global structural properties are not fully understood. Deep imaging of the galaxy in the NIR by Noeske et al. (2003) and the optical by Micheva et al. (2013) suggest the galaxy has an extended red halo around the central starburst. Corbin et al. (1993) published a de Vaucouleurs SB profile fit to V band data from $6.75''$ to $40''$; here we present fits to higher quality imaging data covering a larger radial extent. The total dynamical mass of the galaxy was estimated from poorly resolved HI kinematics to be $2.9 \times 10^9 / \sin^2 i M_\odot$ within 2.1 kpc and the total gas mass is $\sim 7 \times 10^8 M_\odot$ (Kobulnicky et al. 1995; Kobulnicky & Martin 2010). Here we investigate the extended structure of Henize 2-10 by fitting Sérsic functions to its SB profiles based on ground-based imaging data in g - and r -bands.

Many kinematic observations have also been made of the starburst region of Henize 2-10. The gas and stellar kinematics show dramatically different components. The gas is clearly rotating within the central $8''$ as traced by HI, CO and NIR molecular lines (Kobulnicky et al. 1995; Santangelo et al. 2009; Cresci et al. 2010). The rotation speeds are as high as $30 - 80 \text{ km s}^{-1}$, while the velocity dispersion of this component is typically $< 50 \text{ km s}^{-1}$. On the other hand, the stellar component within the central $6''$ is non-rotating and dispersion dominated (Marquart et al. 2007). The velocity dispersion of this component is $\sim 45 \text{ km s}^{-1}$ which implies a dynamical mass of $\sim 6 \times 10^8 M_\odot$ within the central $6''$. We investigate the global and internal kinematics of the SSCs within the nucleus using Gemini/NIFS observations.

Because of the coexistence of a BH and SSCs in the central 100 pc of Henize 2-10, we expect they may migrate to the center due to dynamical friction and form a NSC. This idea was first introduced to explain the nucleus of M31 (Tremaine et al. 1975), and more recently has been re-examined in the context of dwarf elliptical galaxies (Lotz et al. 2001), spiral galaxies (Milosavljević 2004) and in the presence of a massive BH (Antonini et al. 2012; Antonini 2013, 2014). In order to examine this phenomenon in the context of Henize 2-10, we examine the SSC masses, combining the NIFS and archival *Hubble Space Telescope* (*HST*) imaging to model their dynamical friction timescales.

This paper is organized into 6 sections. In Section 2, we describe the observations and data reduction. The extended structure of Henize 2-10 will be discussed in Section 3. Our results on the future of the SSCs at the center of Henize 2-10 are presented in Section 4. In Section 5,

we examine the NIR spectroscopy data and report a possible signature of the BH accretion based on $\text{Br}\gamma$ luminosity. We conclude in Section 6. We assume a distance to Henize 2-10 of 9 Mpc (Méndez et al. 1999); the physical scale assuming this distance is $\sim 43 \text{ pc } ''^{-1}$. Unless otherwise indicated, all quantities quoted in this paper have been corrected for a foreground extinction $A_V = 0.306$ ($A_g = 0.369$, $A_r = 0.255$; Schlafly & Finkbeiner 2011).

2. DATA AND DATA REDUCTION

2.1. Magellan/Megacam data

Images of Henize 2-10 were taken on Nov. 21, 2011 with Megacam on the Magellan/Clay telescope. The seeing was poor ($1.5-2''$), but the night was photometric. Five 100s exposures were taken in g -, r -, and i -band at an airmass of ~ 1.15 ; the i band data suffered from fringing and poor sky subtraction and thus was not used in our analysis. The images were dithered to remove the chip gaps. Final, flat-fielded images were created by the pipeline at the Smithsonian Astrophysical Observatory Telescope Data Center; we made further corrections to the sky subtraction on each chip to ensure a flat field. Specifically, we fit a gradient to the residual background in each chip to a linear function along the horizontal direction and subtracted this off. We then matched the background in neighboring fields to ensure as flat a field as possible before combining the images using *Swarp* (Bertin et al. 2002). Flux calibration was obtained through observations of equatorial SDSS fields in each band, and are thus on the SDSS system.

2.2. Gemini/NIFS data

Gemini/NIFS data of Henize 2-10 was taken in April 2010 using Altair adaptive optics for a program (PI: Usuda) to examine the SSCs and gas conditions within the galaxy. We downloaded the K -band data and accompanying calibration observations from the Gemini Science Archive. The total data included 9 on-source and 9 off-source exposures, each with an exposure time of 300s. The data were taken at airmass between 1.5 and 1.9. Data reduction was performed as outlined by Seth et al. (2010), with telluric calibration performed using an AOV star (HIP45037) taken at similar airmass. Flux calibration of the spectroscopic cube was performed by using a zeropoint derived from telluric stars and a 2MASS K_s filter response curve; the flux calibration is expected to be good to $\sim 10\%$. Final cubes were constructed from 8 of the 9 sky-subtracted on-source cubes with good image quality. The line spread function in each pixel was determined by using a sky cube created with the same dither pattern as the science data cube; the median FWHM is 4.15\AA ($R \sim 5500$), with a variation from 3.4 and 4.9\AA across the map. The FWHM of the AO corrected PSF in the final cube is quite good; the brightest SSC, which we refer to as CLTC1 following Chandar et al. (2003), has a measured FWHM of $\sim 0''.24$. From *HST/HRC* images (§2.3), we measured a true FWHM of $\sim 0''.19$, suggesting the true PSF is $\sim 0''.15$ FWHM (3 pixels in our final cubes). The signal-to-noise ratio (SNR) per pixel ranges from 5-65 across the cube. The NIFS data cubes were astrometrically aligned to previous measurements using *HST* data aligned to 2MASS astrometry as in Reines et al. (2011). The absolute error

in astrometry is thus $\lesssim 0''.1$, and the astrometric error relative to the nuclear X-ray source is $0''.13$ in RA and $0''.33$ in Dec, while the alignment of the nuclear radio source is $< 0''.1$ (supplementary materials; Reines et al. 2011). All velocities are corrected to the barycentric velocity; the correction applied was -20.35 km s^{-1} .

2.3. *HST* data

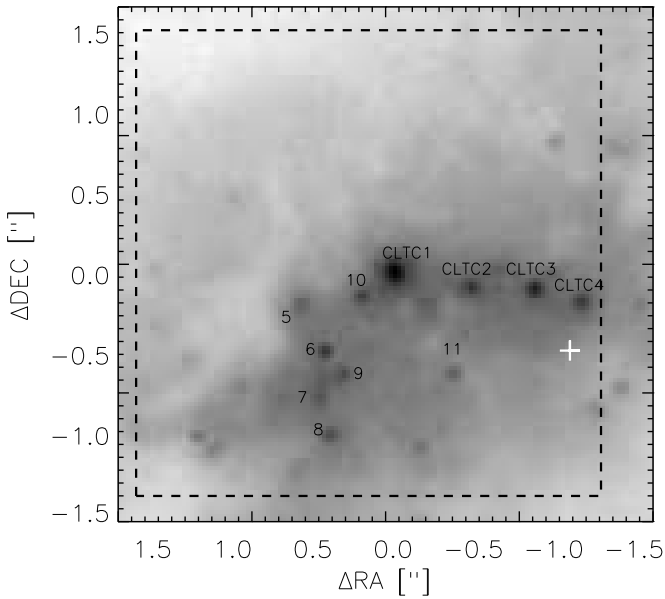


FIG. 1.— *HST* ACS/HRC *F814W* of the central region of Henize 2-10. The 11 SSCs in our sample are labeled. CLTC1-4 have been previously identified in Chandar et al. (2003); the other clusters are identified in this paper and are labeled with numbers 5-11 (see Table 3 for RA and Dec positions). The dashed black box is the Gemini/NIFS field of view. The white cross indicates the BH's position. The position is given relative to RA = $08^h 36^m 15^s.199$, Dec = $-26^\circ 24' 33''.62$.

We use *HST* data in two filters in this paper: (1) *ACS/HRC* data in the *F814W* filters taken in November 2005 (Program ID: 10609, PI: Vacca) and (2) *NICMOS NIC2* data in the *F205W* filter taken in October 2006 (Program ID: 10894, PI: Johnson). Due to the high resolution of the *F814W* data, we used it to select the brightest star clusters in the starburst region as shown in Fig. 1. These images are used in combination with the Gemini/NIFS data to determine the masses of SSCs and their possible dynamical friction timescales of forming an NSC at the center of Henize 2-10 (§4).

2.4. Stellar Kinematics of Gemini/NIFS data

We used the procedure described in Seth et al. (2010) to derive stellar kinematics in the central starburst region of Henize 2-10. Before deriving kinematics, we bin spectra using the Voronoi binning method (Cappellari & Copin 2003) to ensure a signal-to-noise, SNR, of ~ 25 in each bin. Next, we determined the radial velocity, v , the velocity dispersion, σ , the skewness, h_3 , and the kurtosis, h_4 , in the wavelength region from $2.28 \mu\text{m}$ to $2.40 \mu\text{m}$ including the position of CO absorption bandheads by using the PPXF code of

Cappellari & Emsellem (2004). This code requires stellar templates; we used high resolution templates from Wallace & Hinkle (1996) of eight stars with spectral types between G and M and including all luminosity classes. The program finds the best matching template from the set of templates, convolves them with the line spread function determined from fits to sky lines in each pixel, and finds the best light-of-sight velocity distribution (LOSVD) which is described in term of Gauss-Hermite series. Errors on the LOSVD are calculated from Monte Carlo simulations adding in Gaussian random error to each pixel and redetermining the velocities. These radial velocity and dispersion errors range from 0.3 km s^{-1} to 25 km s^{-1} ; we note that systematic errors due to sky and background subtraction, telluric correction, and template mismatch are likely of order a few km s^{-1} ; more discussion of the systematic errors is presented in §4.2. Based on visual inspection, errors in dispersion larger than 20% were unreliable, and therefore we eliminate these bins from our analysis. Although we do not cover the full central region, the median velocity in the higher SNR regions of our maps is 876 km s^{-1} or $\sim 4 \text{ km s}^{-1}$ offset from the systemic velocity of $872 \pm 6 \text{ km s}^{-1}$ given by Marquart et al. (2007). We therefore use the Marquart systemic velocity value throughout this paper.

Fig. 2 shows the velocity and dispersion maps of the stellar component derived from the CO bandhead. We note that our data do not cover the entire nuclear region of Henize 2-10; the expected location of the BH is near the western edge of our maps and is marked by a red cross in Fig. 2. No peak in total intensity or change in dispersion or velocity is seen at the location of X-ray and radio source associated with the BH.

The kinematic maps show two distinct regions. The stars clusters are blue shifted relative to the surrounding stars by 20 km s^{-1} to 30 km s^{-1} . The dispersions in these regions are low, $\lesssim 30 \text{ km s}^{-1}$. The clusters are apparently rotating in the same sense as the gas component (Cresci et al. 2010), with an amplitude somewhat less than the gas. Outside of the clusters, the kinematics have a higher dispersion of $\sim 45 \text{ km s}^{-1}$ and don't appear to have strong rotation. The kinematics of these non-cluster stars are consistent with the lack of rotation and $\sim 45 \text{ km s}^{-1}$ dispersion observed over the central $6''$ region by Marquart et al. (2007). Thus it appears the dispersion profile of the non-cluster component within the inner $\sim 6''$ is nearly flat. We note that in the central region where we are observing, the seeing limited measurements of Marquart et al. (2007) find a dispersion of $\sim 28 \text{ km s}^{-1}$, likely due to the influence of the lower dispersion star clusters. We discuss dispersion measurements of the most massive cluster, CLTC1, in §4.2.

3. EXTENDED STRUCTURE

3.1. SB Profiles

To examine the extended structure and nature of Henize 2-10, we constructed SB profiles from the *g*- and *r*-band Magellan/Megacam images (§2.1). We first masked out all foreground stars and background galaxies by using SEXTRACTOR (Bertin & Arnouts 1996) to determine the shape, size, and position of each source. Each object's size was increased by a factor of 2 while

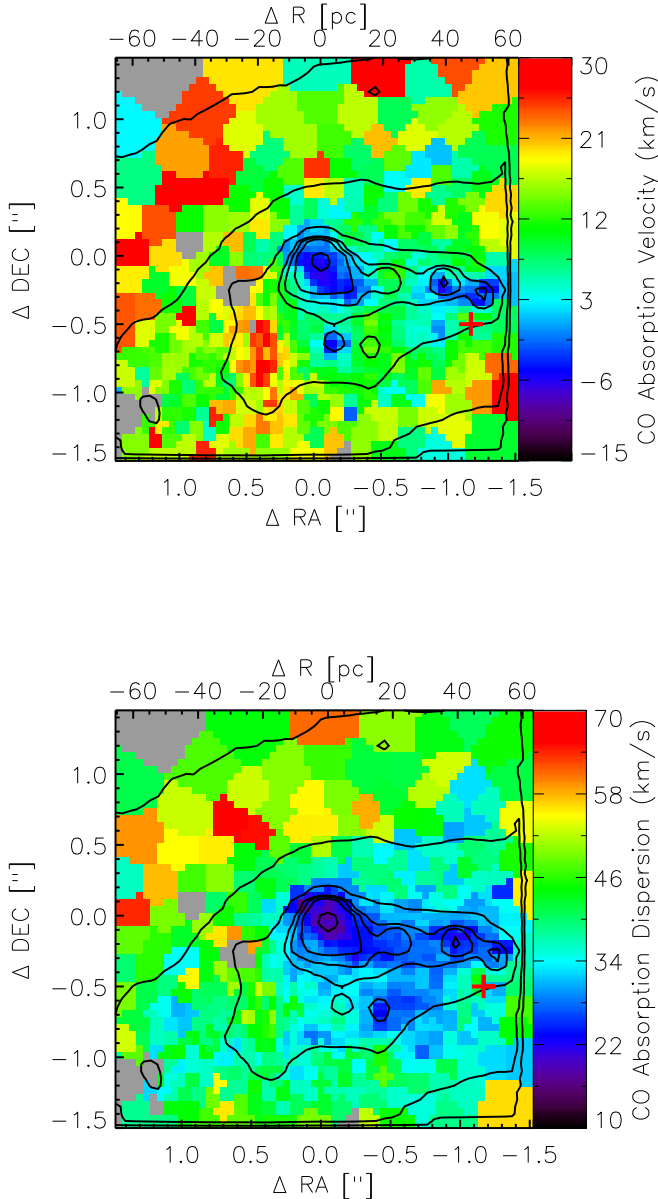


FIG. 2.— Velocity map (Upper Panel) and dispersion map (Lower Panel) of the stellar component derived from the CO absorption line bandhead. The radial velocity is shown relative to the systemic velocity derived by Marquart et al. (2007) of 872 ± 6 km s $^{-1}$. The contours show the K band image continuum with contours at surface brightness of 15.7, 15.9, 16.1, 16.6, 17.7 mag/arcsec 2 . The red cross marks the location of the BH. The positions are given relative to CLTC 1 (Table 3).

masking. The SB profiles were then derived using the IRAF `ellipse` routine to extract fluxes, major semiaxis, etc. While extracting the fluxes, we use the best fit position angle and ellipticity from Micheva et al. (2013); the ellipticity is fixed at $e = 0.15$, and the position angle is fixed at $PA = 28^\circ$. The Magellan r -band images with the contours are presented in Fig. 3. The r -band SB profile is shown in Fig. 4. The total luminosity of the galaxy

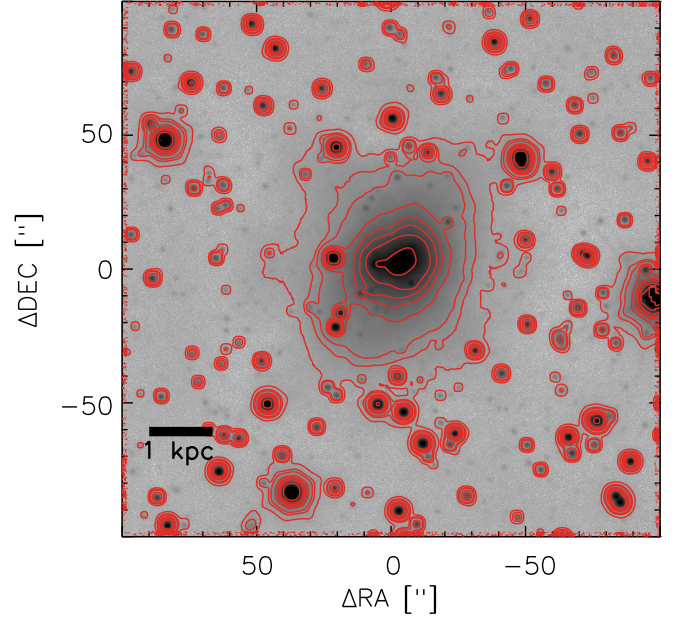


FIG. 3.— Contour plot based on the Megacam r -band image of Henze 2-10. The red contours are at a surface brightness $\mu_r = 18.5, 19.5, 20.0, 20.7, 21.5, 22.5,$ and 23.5 mag/arcsec 2 .

in g - and r -band between $0''$ and $100''$ is $\sim 5.8 \times 10^9 L_\odot$ and $\sim 6.3 \times 10^9 L_\odot$. The effective (half-light) radius of the overall galaxy is $30''.0$ (1.3 kpc) and $32''.0$ (1.4 kpc) in g - and r -band, respectively.

The central most region of Henze 2-10 is dominated by a young starburst; to focus on the extended structure and minimize the affect of this starburst we only fit the profile beyond $2''$. We note that because our PSF FWHM is smaller than this radius, the affects of the PSF on our SB profile fits are minimal. The outer boundary of our fits are set by the error in our sky subtraction; this uncertainty in the sky subtraction is shown by black solid lines in Fig. 4; beyond $70''$ the sky subtraction makes the SB profile less reliable. The outer parts were fit by a double-Sérsic profile for both g - and r -images from $2''$ (86 pc) to $100''$ (4.3 kpc) from the center. Here we used the non-linear least squares IDL MPFIT function to implement the fitting procedure. Henze 2-10's (SB) profile in both bands is best fit by two Sérsic components, an inner component with $n \sim 0.6$ and $r_{\text{eff}} \sim 6''$ (260 pc) and an outer component with $n \sim 1.8$ and $r_{\text{eff}} \sim 25''$ (1 kpc). The full results and errors in each band are shown in Table 1. Fig. 4 shows both the best double- and single-Sérsic fit profiles in r -band. The single-Sérsic fit to the r -band image provides a worse fit, but has $n = 4$ (a de Vaucouleurs profile) and $r_{\text{eff}} = 12.5''$ (538 pc). In addition to having larger residuals, the single-Sérsic fit (1) does not well match the observed color profile, (2) the χ^2 are $\sim 25\%$ larger than that of the double-Sérsic profiles, and (3) over-predicts the amount of light even with the overlying starburst component at the center of the galaxy. Therefore we prefer the double-Sérsic fit and use this fit throughout the paper. We note that while Corbin et al. (1993) do not provide the effective radius of their fits, both our single and double-Sérsic fits are better fits to the data than the de Vaucouleurs profile fit

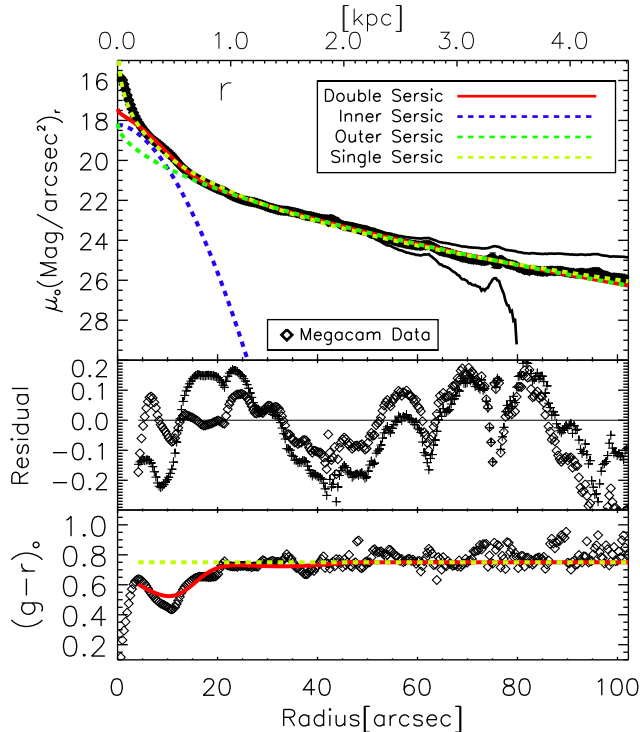


FIG. 4.— *Upper Panel:* The r -band SB profile of Henize 2-10. Data points show the measured profile with the black lines showing the systematic uncertainty due to sky subtraction. The best-fit double-Sérsic model is shown in red and the best-fit single-Sérsic model is shown as a dashed yellow line. The individual components of the Double-Sérsic model are shown as dashed blue and green lines. We note that the inner $2''$ region is excluded from the fit and the profiles in this region are extrapolated from the best fits. *Middle Panel:* The SB profile residuals after subtraction of the double-Sérsic (diamonds) and the single-Sérsic (pluses) model profiles. *Bottom Panel:* The color profile of Henize 2-10. The black diamonds are the data points from the Megacam data, the red solid line indicates the double-Sérsic component fit, and the yellow dashed line indicates the single-Sérsic component fit applied to both g - and r -bands.

they show in their Fig. 3 of Corbin et al. (1993). Specifically, their fit is poor at radii less than $14''$.

To estimate the effect of our choice of inner and outer boundaries on the fit, we varied the inner boundary from $2''$ to $10''$ and outer boundary from $70''$ to $110''$ for both g - and r -images; this resulted in a variation of the inner Sérsic index and effective radius of 1% and the outer fitted Sérsic SB profile less than 5%. Our results therefore appear robust to the range over which the profile is fitted. The profiles are fit well by the two Sérsic components model, with residuals less than $\sim 20\%$ except for an outer starburst component seen at a radius of $\sim 10''$. The colors throughout the region (except for the starburst) are consistent with a >1 Gyr old population and thus the SB profile we fit appears to describe the older underlying component of Henize 2-10; this is especially true for the outer component, which dominates beyond $\sim 10''$.

To test our results, we compared our profiles with those in Bessel-Johnson $UBVHK$ filters (Micheva et al. 2013) using conversions between Sloan and Johnson filter sets (Fukugita et al. 1996; Smith et al. 2002; Jester et al. 2009). The transformed profiles agree from the center to $90''$ to within 10%, beyond this distance, a somewhat

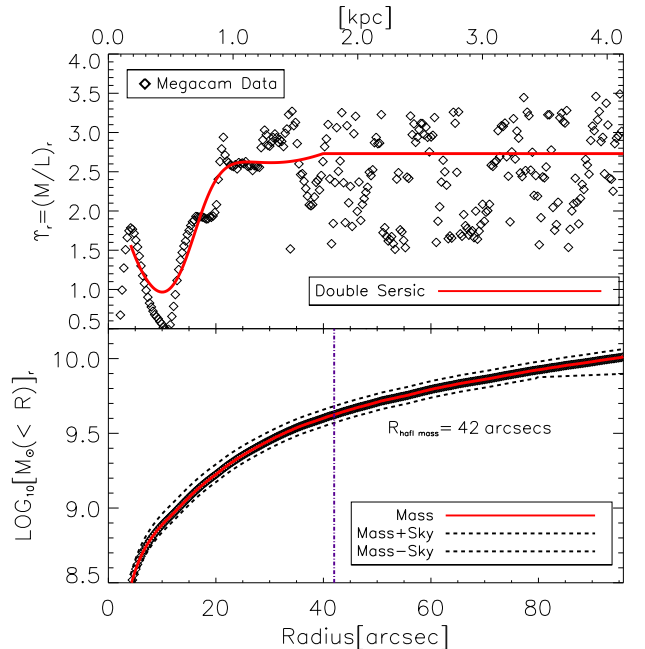


FIG. 5.— *Upper Panel:* The mass-to-light profile in the r -band determined from the colors using the relation of Zibetti et al. (2009), the black diamonds indicates the measured colors while the red solid line shows the results from the two component Sérsic model profile. *Bottom Panel:* The cumulative mass within radius R as determined from the r -band image. The purple vertical line shows the half mass radius. The black diamonds are the mass profile from the data and the red solid line is the predicted mass profile from two component Sérsic fit. The black dashed lines show the uncertainty in the mass due to sky subtraction.

larger systemic discrepancy of $\sim 20\%$ exists between the g - and B -band. This discrepancy does not affect our profile fits which are performed only out to $100''$. We also fit all 5 filters $UBVHK$ in the same range of radii from $2''$ to $100''$ with the similar double-Sérsic profile which we obtained from our g - and r -band data. The profiles fit well with residuals less than $\sim 20\%$ in each band. This suggests that the two component structure we derive from our data is robust.

3.2. Mass-to-Light ratio and Mass

To determine the total mass of Henize 2-10, we split the galaxy into multiple components; for the inner component we derived the mass using kinematics, while at intermediate and large radii, we determined the mass-to-light ratio Υ from the integrated color of the galaxy. These results are summarized in Table 2.

In the outermost of the galaxy beyond $20''$, the color is nearly constant, $(g-r)_0 = 0.75 \pm 0.05$. Using the dependence of mass-to-light ratio, Υ , on the color as describing in Zibetti et al. (2009), we calculated $\Upsilon_g = 3.5 \pm 0.4$, $\Upsilon_r = 2.5 \pm 0.4$, respectively at large radii. The luminosity beyond $20''$ is $L_g = (3.5 \pm 1.3) \times 10^9 L_\odot$ and $L_r = (3.9 \pm 1.3) \times 10^9 L_\odot$ corresponding to a total outer mass of $M_{*,g} = (8.1 \pm 3.6) \times 10^9 M_\odot$ and $M_{*,r} = (7.7 \pm 2.5) \times 10^9 M_\odot$ from the g - and r -band. Due to the large number of foreground sources requiring masking, the uncertainty in the sky background is substantial at large radii (see Fig. 4). This is the dominant source of error in our luminosity estimate and these

TABLE 1
MORPHOLOGICAL TABLE OF HENIZE 2-10

Double-Sérsic Fits					Integrated Data				
Filter	$(r_{\text{eff1}}, r_{\text{eff2}})$ (")	$(r_{\text{eff1}}, r_{\text{eff2}})$ (pc)	(μ_{e1}, μ_{e2}) [mag/'' ²]	(n_1, n_2)	Υ (Outer Comp.)	M [mag]	L ($\times 10^9 L_\odot$)	Mass ($\times 10^9 M_\odot$)	Υ_{ave}
(1)	(2)	(3)	(4)	(5)	(6)	(7)	(8)	(9)	(10)
g	6.04 ± 0.07 24.72 ± 0.21	259 ± 3 1063 ± 9	18.7 ± 0.2 22.0 ± 0.2	0.58 ± 0.01 1.70 ± 0.01	3.5 ± 0.5	-19.2 ± 0.2	5.77 ± 1.63	10.3 ± 3.9	1.8 ± 0.2
r	5.97 ± 0.07 24.63 ± 0.20	257 ± 3 1060 ± 9	19.3 ± 0.3 22.1 ± 0.2	0.57 ± 0.01 1.80 ± 0.01	2.5 ± 0.4	-19.8 ± 0.4	6.25 ± 1.78	9.8 ± 3.0	1.6 ± 0.2

NOTE. — NOTES: The morphological characteristics of Henize 2-10 in two ground-based images; column (1): g - and r -band images; column (2): effective radii in arc second; column (3): effective radii in pc; column (4): effective SB (at the position of effective radii); column (5): Sérsic indices; column (6): outer mass-to-light ratios; column (7): absolute magnitudes; column (8): total integrated luminosity under the double-Sérsic profiles of the outer components; column (9): total stellar integrated mass under the double-Sérsic profiles of the inner and outer components combined with the mass of the starbursting region ($2''$); column 10: the average mass-to-light ratios of the whole galaxy from $0''$ to $100''$ including three components: inner starbursting region (from $0''$ to $2''$), intermediate and large radii region of the double-Sérsic profiles from $2''$ to $100''$.

TABLE 2
MASS & LIGHT DISTRIBUTION REGIONS TABLE OF HENIZE 2-10

Radius (")	L_g ($\times 10^9 L_\odot$)	L_r ($\times 10^9 M_\odot$)	M_{dyn} ($\times 10^9 M_\odot$)	$M_{\text{pop},g}$ ($\times 10^9 M_\odot$)	$M_{\text{pop},r}$ ($\times 10^9 M_\odot$)
(1)	(2)	(3)	(4)	(5)	(6)
0–2	1.43 ± 0.22	1.40 ± 0.24	0.27 ± 0.11	–	–
2–6	0.19 ± 0.03	0.21 ± 0.03	0.37 ± 0.15	0.36 ± 0.12	0.35 ± 0.14
6–20	0.65 ± 0.13	0.74 ± 0.17	–	1.53 ± 0.13	1.50 ± 0.12
20–100	3.46 ± 1.26	3.88 ± 1.34	–	8.10 ± 3.61	7.72 ± 2.54

NOTE. — NOTES: The mass and light distribution regions of Henize 2-10 in two ground-based images; column (1): four distinct regions with different mass and light distributions; column (2): the total integrated luminosities in each region of g -band; column (3): the total integrated luminosities in each region of r -band; column (4): the dynamical mass of each region derived from the linear relation as Marquart et al. (§3.1 2007); column (5): the stellar population mass of each region in g -band; column (6): the stellar population mass of each region in r -band. Here the symbol – means we do not have the corresponding calculation values for that case. Beyond the radius of $6''$ the linear relation as in Marquart et al. (§3.1 2007) is invalid to calculate the stellar dynamical mass, then we only used the stellar population mass.

errors are included in the luminosity and mass uncertainties listed in Tables 1 and 2.

At intermediate radii, between $6''$ and $20''$, the color and thus the mass-to-light ratio varies significantly. The annulus colors, $(g-r)_0$, are converted into annulus mass-to-light ratios using the Zibetti et al. (2009) relations. These vary between 1.0 and 2.5 in r -band and vary between 1.0 and 3.5 in g -band. The total mass between $2''$ and $20''$ are $\sim (1.89 \pm 0.25) \times 10^9 M_\odot$ and $\sim (1.85 \pm 0.26) \times 10^9 M_\odot$ for g - and r -band. The error bars on these data points include the uncertainty on integrated luminosity within this annulus and the scatter $(g-r)_0$, which are converted into the mass-to-light ratio uncertainties (Zibetti et al. 2009).

Between radii of $2''$ and $6''$, we can estimate masses using both the photometric method we used at larger radii, and kinematic estimates. We estimate the virial

mass based on the dispersion in the inner $6''$ of $45 \pm 4 \text{ km s}^{-1}$ measured by Marquart et al. (2007) and their virial mass estimator. We derive a mass $(3.7 \pm 1.5) \times 10^8 M_\odot$ between $2''$ and $6''$. This dynamical mass agrees well with the photometric mass estimates in this same annulus (Table 2); for our final calculations we use the r -band based photometric mass within this annulus.

Because of the lack of resolution in our Megacam images, the inner color and SB profile within $2''$ from the center of Henize 2-10 are difficult to determine. Therefore, we obtained an estimation of the mass of the inner starburst component from kinematics. Our Gemini/NIFS kinematics show the constant 45 km s^{-1} dispersion seen by Marquart et al. (2007) continues to within the central $2''$. This corresponds to a dynamical mass of $(2.7 \pm 1.1) \times 10^8 M_\odot$ within $2''$, which we can add to our photometric estimates from larger radii. The r -band

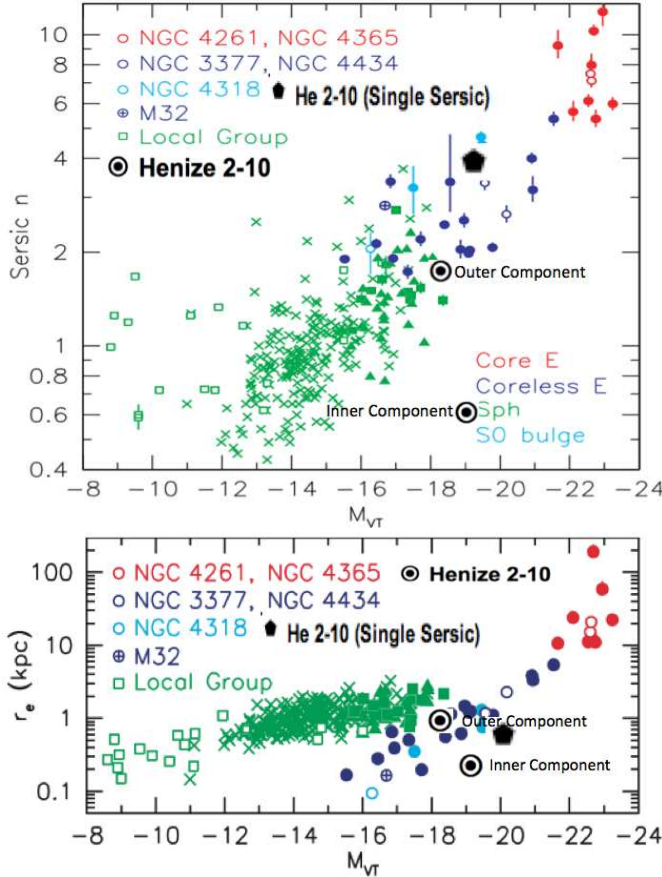


FIG. 6.— The properties of early-type galaxies as taken from Kormendy et al. (2009), Fig. 33 and 37. *Upper Panel:* The top plot shows the correlation between Sérsic index n and M_{VT} . *Bottom Panel:* The correlation of the effective radius, r_e , and M_{VT} . The M_{VT} of Henize 2-10 was converted from the absolute magnitude in g - or r -band (Fukugita et al. 1996; Smith et al. 2002; Jester et al. 2009). The symbols in both panels are the same: Henize 2-10 is indicated with a bulls-eye, red points are core Es, blue points are extra light Es, green points are Sph galaxies, and turquoise points are S0 bulges as discussed in Kormendy et al. (2009). The green triangles show spheroidals from Ferrarese et al. (2006b). The crosses show spheroidals from Gavazzi et al. (2005). The open squares are for Local Group spheroidals Caldwell (1999). The open symbols are non-Virgo Cluster galaxies.

luminosity of this region is $L_{r,2''} = (1.40 \pm 0.24) \times 10^9 L_\odot$, and therefore the mass-to-light ratio in this region drops to $\Upsilon_{r,2''} = (0.19 \pm 0.08)$ as we might expect for a young population.

Summing the different radial components in Table 2 together, Henize 2-10 has a total luminosity within $100''$ (4.3 kpc) of $L_r = (6.3 \pm 1.8) \times 10^9 L_\odot$ ($M_r = -19.8 \pm 0.4$). The total stellar mass in this aperture is $M_{*,r} = (9.8 \pm 3.0) \times 10^9 M_\odot$, corresponding to an average mass-to-light ratio of $\Upsilon_r = (1.6 \pm 0.4)$. Fig. 5 shows the resulting mass and mass-to-light ratio profile of the galaxy in the r -band, Υ_r including the dominant error from the sky determination. The $100''$ aperture may not enclose all the galaxy’s light and mass; integrating our SB profile fits to infinity yields $M_r = -19.9$ or about 10% more light than within our aperture. The mass derived from g -band is consistent within the errors with the r -band mass. Due to the reduced effects of extinction and the good match of our r -band profile to the Micheva et al. (2013) pro-

files, we quote final numbers on the mass based on the r -band data. We note that while the inner starburst region ($r < 2''$) contributes about 23% of Henize 2-10’s r -band luminosity, it contributes about $\sim 3\%$ to the total stellar mass of the galaxy.

A dynamical estimate of Henize 2-10’s total mass within 2.1 kpc was derived from HI kinematics to be $2.7 \times 10^9 / \sin^2 i M_\odot$ by Kobulnicky et al. (1995). Our mass estimate within this same aperture is $6.4 \times 10^9 M_\odot$ from r -band, thus implying inclinations of $i \sim 38^\circ$. This translates into an expected ellipticity of $e \sim 0.2$ assuming a thin disk. This is consistent with the ellipticity of 0.15 of the outer isophotes in our ellipse fits and that of Micheva et al. (2013), suggesting that the gas disk is aligned with the outer stellar component.

Other previous photometric mass estimates of Henize 2-10 (Kormendy & Ho 2013; Reines et al. 2011) have suggested a lower mass for Henize 2-10 $\sim 1.4 - 3.7 \times 10^9 M_\odot$ with factor of 3 uncertainties. These estimates are based on K-band absolute magnitudes derived from Noeske et al. (2003) $M_{Ks} = -20.86$ over an unspecified aperture and from 2MASS $M_{Ks} = -20.81$ (Skrutskie et al. 2006). These translate to a K_s -band luminosity of $\sim 5 \times 10^9 L_\odot$. Comparing our integrated magnitudes, the color is $r - K_s \sim 1.1$, bluer than expected for a predominantly old population. However, the color at radii beyond $\sim 10''$ between our data and Noeske et al. (2003) is $r - K_s \sim 2.3$ and the profile appears to get redder in the inner part of the galaxy likely due to hot dust; thus it appears the integrated K_s -band luminosities are underestimated. This may be due to use of a smaller aperture than our data. We also note that K_s band M/L_s are more uncertain than optical M/L_s due to the poorly understood contributions of supergiant and AGB stars (e.g., Zibetti et al. 2009; Melbourne et al. 2012).

Although we cannot separate out the masses of the two best-fit Sérsic components exactly, we use the Υ_r profile to estimate the mass for both components. For the inner component, the integrated luminosity and the average mass-to-light ratio are $L_{r,in} = (3.1 \pm 0.3) \times 10^9 L_\odot$ ($M_{r,in} \sim -19.1$), thus the inner component mass is $M_{*,r,in} = (3.9 \pm 0.6) \times 10^9 M_\odot$. Similarly, we obtained the integrated luminosity $L_{r,out} = (2.3 \pm 0.4) \times 10^9 L_\odot$ ($M_{r,out} \sim -18.4$), and the mass $M_{*,r,out} = (5.8 \pm 1.2) \times 10^9 M_\odot$ for the outer component.

3.3. Henize 2-10 in context

Apart from the central starburst component, Henize 2-10 appears to be an early-type galaxy. This is suggested by (1) its central dispersion dominated kinematics (our Fig. 2 and Marquart et al. 2007), (2) the consistently red color of its outskirts. We argue below that its outer component Sérsic index ($n \sim 1.8$) is also consistent with this interpretation.

It is useful to compare the morphology and luminosity of Henize 2-10 to other early-type galaxies to better understand its nature and whether or not the presence of a massive BH is suprising. To facilitate this comparison, we placed our fitted models on diagrams of early-type galaxies from Kormendy et al. (2009). We plotted each component of our double-Sérsic fits on the plot of absolute magnitude vs. Sérsic n and effective radius;

the inner component is clearly an outlier component in both plots, but the outer component lies at the boundary between what Kormendy considers spheroidal and elliptical galaxies. One possible interpretation of this is that Henize 2-10 was a typical early-type galaxy before some event formed the nuclear component. If this is the case, the stellar populations even outside the nucleus should be somewhat younger than the surrounding envelope. In the future, this may result in an age gradient similar to that seen in M32 (Worthey 2004) and other lower mass early-type galaxies (e.g., Cid Fernandes et al. 2005; Koleva et al. 2009, 2011; Toloba et al. 2014). We can also consider the galaxy as a single component (despite a worse fit to the profile), in which case our single-Sérsic fits place it firmly amongst the elliptical galaxies with a high Sérsic index.

Assuming our preferred two component model, the outer component is typical of an old early-type galaxy. The inner component, with its varying M/L , likely represents more recent star formation (perhaps the older portion of the current central starburst), and thus its position off the early-type galaxy locus is unsurprising. The single component fit overpredicts the flux in the center. Given that most of this flux is in a young starburst it is clear that a single $n=4$ Sérsic profile does not accurately describe the old population or mass profile of the galaxy. The effective radius and Sérsic index therefore are unlikely to indicate much about its physical origin.

In the context of Henize 2-10 being a relatively massive $\sim 10^{10} M_\odot$ early-type galaxy, it is not surprising that Henize 2-10 hosts a BH. While dynamical evidence for BHs in galaxies of this mass is almost non-existent (McConnell & Ma 2013), AGN in this mass range and lower have been found (Greene & Ho 2007; Barth et al. 2008; Desroches & Ho 2009; Gallo et al. 2010; Reines et al. 2013, 2014). Analyzing these observations, Greene (2012) and Miller et al. (2014) suggest that the occupation fraction of BHs in early-type galaxies around $10^{10} M_\odot$ is high, $\sim 90\%$. This implies that the BH may be a pre-existing object, and not a result of the intense starburst taking place in the galaxy.

Finally, Henize 2-10 appears to be very isolated, with no known companions within $v < 2000 \text{ km s}^{-1}$ and 2 degrees ($\sim 0.3 \text{ Mpc}$) of the galaxy. Thus the most plausible explanation for Henize 2-10's relatively steep Sérsic index and current starburst is that it is a late stage merger of two other smaller galaxies as suggested by Kobulnicky et al. (1995) and Marquart et al. (2007).

4. THE FATE OF THE NUCLEUS

Henize 2-10 contains several super star clusters (SSCs) in the central starburst region (Kobulnicky et al. 1995; Méndez et al. 1999; Johnson et al. 2000; Vacca et al. 2002; Chandar et al. 2003) and a massive BH with approximative mass of $\sim 10^6 M_\odot$ (with an uncertainty of a factor of ~ 10) at its center (Reines et al. 2011). We expect the BH and SSCs' orbits to decay due to the gravitational interaction with the surrounding galaxy. There are two popular models of NSC formation: (1) dissipative model where the NSC forms *in situ* from gas accreted into the center and (2) the dissipationless model where migration of massive star clusters to the center forms the NSC (Chandrasekhar 1943; Tremaine et al. 1975; Merritt et al. 2004; Just & Jahreiß 2010; Antonini

2013).

The lack of an existing NSC combined with the presence of a large number of massive young clusters suggests that Henize 2-10 may be an example of ongoing dissipationless nuclei formation. We examine the expected dynamical friction timescale of this merging in this section based on models by Antonini (2013). Assuming that SSCs have King density profiles, orbit within a galaxy with a power-law profile $\rho(r) = \rho_0(r/r_0)^{-\gamma}$, and accounting for mass loss due to the galactic tidal field, the dynamical friction timescale for SSCs to reach the center of the galaxy from dynamical friction mechanism is (Eq. 32 of Antonini 2013):

$$\tau_\star = 3 \times 10^{10} \text{ yr} \frac{(4-\gamma)\sqrt{\gamma} \ln \Lambda_3^{-1}}{(3-\gamma)^3 F(\gamma)} \rho_{0,5} r_{0,700}^3 \sigma_{K,10}^{-3} \left(\frac{r_{\text{in}}}{r_0} \right)^{3-\gamma} \quad (1)$$

with the central density, $\rho_{0,5} = \rho_0/5 M_\odot \text{ pc}^{-3}$, the scale radius, $r_{0,700} = r_0/700 \text{ pc}$, the Coulomb logarithm, $\ln \Lambda_3 = \ln \Lambda/3$, the cluster mass, $m_{cl,6} = m_{cl}/10^6 M_\odot$, the central dispersion velocity of SSC, $\sigma_{K,10} = \sigma_K/10 \text{ km s}^{-1}$, and the initial distance, r_{in} , of the SSC from the galactic center. The γ dependent coefficient, $F(\gamma) = (0.193, 0.302, 0.427)$ for $\gamma = (1, 1.5, 2)$ corresponding to the analytical formula can be found in (Merritt et al. 2004).

$$F(\gamma) = \frac{2^\beta \Gamma(\beta)(2-\gamma)^{-\gamma/(2-\gamma)}}{\sqrt{2\pi} \Gamma(\beta-3/2)} \int_0^1 y^{1/2} \left(y + \frac{2}{2-\gamma} \right) dy \quad (2)$$

where $\beta = (6-\gamma)/2(2-\gamma)$. $\ln \Lambda$ has a value from 2 to 7 (Agarwal & Milosavljević 2011).

We note that the equation (1) does not take into account the presence of a BH; however, given the low mass ($\sim 10^6 M_\odot$) and small sphere of influence (a few pc) of the BH, clusters should reach a radius similar to the size of typical NSCs before feeling the effects of the BH.

We also caution that in some cases, dynamical friction appears to be less efficient than predicted from theory. Most notably, Lotz et al. (2001) suggest that the faintness of nuclei in low mass dE galaxies ($M_V > -14$) indicates inefficient dynamical friction, perhaps due to supernova feedback or mismatches of the dark matter halo with the visible baryonic component. Given the much higher luminosity of Henize 2-10 and the likely dominance of baryonic matter near the center of the galaxy, it is in a regime where Lotz et al. (2001) find evidence for dynamical friction working as expected.

We apply these dynamical friction timescale results to explore the possibility of forming a NSC at the center of Henize 2-10 due to the migration of SSCs. Before we can do this, we need to determine several parameters for the galaxy and clusters, which we do in the following subsections. This includes a determination of the cluster galactocentric positions, profiles, and masses, as well as the density profile of the galaxy. We derive these properties using a combination of high resolution *ACS/HRC* imaging and Gemini/NIFS spectroscopy.

4.1. Determination of Cluster photometric parameters, description of the cluster sample

We identified the brightest 11 SSCs in the nuclear region using the *HST* images as shown in Fig. 1. These

clusters are also seen in the Gemini/NIFS observations, but are not as well resolved; the brightest four clusters are clearly visible in both data sets and allow us to astrometrically align our Gemini/NIFS image with the *HST* data.

Four of the SSCs identified here were previously identified by Chandar et al. (2003); we label these CLTC1-4. The brightest SSC is CLTC1, and this cluster is shown at the center of our maps. Seven other bright SSCs are also identified in the *HST* imaging, and we number these 5 through 11. The coordinates of all clusters are given in Table 3. For purposes of our dynamical friction timescales calculation, we assumed the galactocentric radius of the clusters is their projected distance to the BH. Given the compact region over which clusters are found, it is likely that this distance is within $\sim 50\%$ of their true galactocentric distance.

For all 11 clusters, we performed King model fits to the *HST ACS/HRC F814W* images. We followed the procedure described in Larsen (2001) assuming concentration parameter, $c = 30$. We fit the data with the *iSHAPE* routine which is part of the *BAOLAB* software (Larsen 1999). To fit each SSC's size (the core radius or effective radius) in the image, *iSHAPE* needs a corresponding PSF, and a charge diffusion kernel image. The PSF is generated by the *Tiny Tim* routine (Krist et al. 2011) and oversampled by a factor of 10 for use with *iSHAPE*. The charge diffusion kernel is generated from header file of distorted PSF image when we ran the *tiny3* task of *Tiny Tim* routine. The core radius, r_c , and effective radius, r_e , from the best fit King model are shown in column 4 and 5 of Table 3. Integrated fluxes of the clusters in both *F814W* and *F205W* are calculated using aperture photometry (see §4.2). The luminosity in *F814W* is given in column 6, while the color *F814W* – *F205W* in VEGA system of integrated fluxes of the two bands is given in column 9. This color is useful for evaluating the similarities in stellar population and reddening among the clusters (see §4.3).

4.2. Virial SSC mass determination

Chandar et al. (2003) estimated masses of the 4 brightest SSCs, CLTC1-4, using stellar population model fits of ultraviolet and blue *HST/STIS* spectra, finding a mass for CLTC1 of $\sim 4.5 \times 10^5 M_\odot$. However, these fits have significant uncertainties due to dust extinction. Here, we measured the dispersion of the brightest cluster, CLTC1, from our Gemini/NIFS data and used it to determine a more robust virial mass estimation (e.g., Peterson & King 1975; Larsen et al. 2002; McCrady & Graham 2007; Strader et al. 2009). We could only determine the internal dispersion of CLTC1 because of galaxy contamination in the other fainter clusters.

Fig. 7 shows the full spectrum and CO absorption bandhead of CLTC1 from Gemini/NIFS data after subtracting an estimation of the background light of the galaxy. We estimated the galaxy background value by taking the median value of pixels surrounding CLTC1 but avoiding contamination from neighboring clusters. For our Gemini/NIFS data of the SSCs, only the spectrum of CLTC1 was cleanly separated from the surrounding galaxy. Specifically, using annuli surrounding the clusters, we find that the background contamination in

CLTC1 is $\sim 20\%$, while in the rest of the clusters it is $> 45\%$.

As for the galaxy as a whole, we fit the kinematics in the CO absorption bandhead to estimate velocity dispersion of CLTC1 using PPXF (see §2.4). As the cluster is nearly unresolved in our data, we sum the light within an $0''.2$ radius aperture over which the source is well above the galaxy background. Our resulting best-fit dispersion for this spectrum is $\sigma = 20.1 \pm 0.6 \text{ km s}^{-1}$. Given that this aperture extends out $\sim 2\times$ the effective radius of the cluster, we assume that this dispersion is reflective of the cluster's global velocity dispersion σ_∞ , which is used in virial mass estimation. To assess the robustness of this dispersion, we conducted several tests: (1) We determined the dispersion value in just the central pixel of the cluster to be $17.6 \pm 1.6 \text{ km s}^{-1}$. (2) We varied the pixels used for background subtraction and find dispersion results that vary from 17 to 21 km s^{-1} . (3) We fit the data to no dispersion model and find that the resulting reduced χ^2 is higher than the best-fit model by 20%. These tests suggest that our dispersion value is clearly resolved by the data, but that the systematic error is more like $\sim 3 \text{ km s}^{-1}$. The cluster's radial velocity is blue-shifted by 6 km s^{-1} relative to the systemic velocity of the galaxy.

The virial mass is calculated using Strader et al. (2009):

$$M_{\text{vir}} = \frac{7.5\sigma_\infty^2 r_{\text{hm}}}{G} = 4 \times a \frac{\sigma_\infty^2 r_e}{G} \quad (3)$$

where σ_∞ is the global velocity dispersion, r_{hm} is the half mass radius, and $r_{\text{hm}} = 4r_e/3$, r_e is the effective radius or half-light radius. The structural parameter, a , of globular clusters (GCs) is 2.5 (Spitzer 1987). We determined r_{hm} or r_e from King model fits as discussed above. Based on the measured dispersion of CLTC1, we estimated a mass of $2.3 \times 10^6 M_\odot$. Assuming a 3 km s^{-1} error on the dispersion, this translates to a $\sim 28\%$ error ($0.6 \times 10^6 M_\odot$) on the mass.

For CLTC1, Chandar et al. (2003) found a mass of $4.5 \times 10^5 M_\odot$ from their spectral fitting, assuming a Starburst 99 (Leitherer et al. 1999) model with a Salpeter initial mass function (IMF) and with lower and upper masses of 1 M_\odot and 100 M_\odot , respectively. This mass is a factor of $5\times$ lower than our dynamical mass estimate of $2.3 \times 10^6 M_\odot$. This discrepancy could be due to the assumption by Chandar et al. (2003) of a 1 M_\odot lower limit on the IMF mass in their models which will lead to an order of magnitude underestimate in the total stellar mass relative to a Kroupa IMF (Kroupa 2001).

4.3. Masses of other clusters

In this section, we made rough estimates of the masses of the other optically visible clusters in the nuclear region using our derived M/L for cluster CLTC1. While this assumption is an undoubtedly oversimplification, it is a reasonable one for two reasons. First, the star clusters studied in this region have all been found to have ages $< 5 \text{ Myr}$ (Chandar et al. 2003), as might be expected from the prodigious star formation rate of $1.9 M_\odot \text{ yr}^{-1}$ (Méndez et al. 1999; Engelbracht et al. 2005; Calzetti et al. 2007). Second, our measurements of the color (*F814W* – *F205W*) between *F814W* and *F205W* bands (Table 3) in most of the clusters suggests they have

TABLE 3
DYNAMICAL QUANTITIES FOR SSCs

SSCs (1)	σ_{cen} (2) (km s ⁻¹)	σ_{aper} (3) (km s ⁻¹)	r_{eff} (4) (pc)	r_c (5) (pc)	L_{F814W} (6) ($\times 10^7 L_{\odot}$)	M (7) ($\times 10^6 M_{\odot}$)	Υ_{F814W} (8)	$F814W - F205W$ (9)
CLTC1 08 ^h 36 ^m 15 ^s .199 -26°24'33".62	17.6 ± 1.6	20.1 ± 0.6	3.43 ± 0.07	1.27 ± 0.03	3.59 ± 0.93	2.30 ± 0.60	0.06 ± 0.02	2.2
CLTC2 08 ^h 36 ^m 15 ^s .164 -26°24'33".71	13.8 ± 1.2		2.07 ± 0.03	0.77 ± 0.01	1.45 ± 0.56	0.92 ± 0.61		2.0
CLTC3 08 ^h 36 ^m 15 ^s .134 -26°24'34".73	15.4 ± 1.3		2.07 ± 0.09	1.00 ± 0.02	1.78 ± 0.74	1.14 ± 0.78		2.1
CLTC4 08 ^h 36 ^m 15 ^s .113 -26°24'34".80	14.4 ± 1.1		1.89 ± 0.11	0.71 ± 0.05	1.42 ± 0.53	0.91 ± 0.60		1.9
5 08 ^h 36 ^m 15 ^s .245 -26°24'34".81	11.0 ± 1.0		1.42 ± 0.13	0.53 ± 0.07	0.63 ± 0.12	0.40 ± 0.21		1.7
6 08 ^h 36 ^m 15 ^s .234 -26°24'34".10	11.0 ± 1.5		1.42 ± 0.17	0.53 ± 0.04	0.63 ± 0.12	0.40 ± 0.21		1.8
7 08 ^h 36 ^m 15 ^s .236 -26°24'34".40	9.1 ± 1.1		2.38 ± 0.34	0.89 ± 0.21	0.72 ± 0.12	0.46 ± 0.25		2.0
8 08 ^h 36 ^m 15 ^s .231 -26°24'34".63	12.5 ± 0.8		1.24 ± 0.04	0.46 ± 0.02	0.70 ± 0.12	0.45 ± 0.24		1.8
9 08 ^h 36 ^m 15 ^s .225 -26°24'34".26	9.3 ± 0.6		1.00 ± 0.03	0.37 ± 0.01	0.32 ± 0.07	0.20 ± 0.11		2.1
10 08 ^h 36 ^m 15 ^s .216 -26°24'34".76	11.6 ± 1.3		1.45 ± 0.05	0.46 ± 0.02	0.70 ± 0.12	0.45 ± 0.24		2.0
11 08 ^h 36 ^m 15 ^s .173 -26°24'34".25	6.2 ± 0.9		2.21 ± 0.07	0.37 ± 0.01	0.32 ± 0.07	0.20 ± 0.11		1.6

NOTE. — NOTES: Individual cluster data for SSCs identified in Fig. 1. Column (1): Identified, CLTC1-4 corresponds to clusters identified by Chandar et al. (2003), the rest are identified here with coordinates given, column (2): Velocity dispersion from central pixel; column (3): Velocity dispersion in 0''.2 radius; column (4): effective (half-light) radius; column (5): core radius; column (6): $F814W$ Luminosity; column (7): Mass estimate; column (8): mass-to-light ratio; column (9): $F814W - F205W$ color. A dynamical mass and Υ_{F814W} were measured only for CLTC1, all other clusters assumed the same Υ_{F814W} to derive their mass.

similar ages and extinctions because the colors change slightly over the NIFS field of view (FOV) and *HST* data. We noted that colors were calculated from a fixed 0''.2 aperture in each cluster; no correction was made for the differing PSF between the bands; however, the difference in encircled energies for a point source is relatively small (75% in $F814W$, 65% for $F205W$), and likely quite similar for all clusters.

The clusters' luminosities used here are the integrated King model luminosities which are obtained from the *i*SHAPE routine. Each cluster's luminosity is output as a parameter, we then correct for Galactic extinction to get the total luminosity shown in column 6 of Table 3. The mass-to-light ratio of CLTC1 in $F814W$ estimated using the virial mass estimate from §4.2 gives a $\Upsilon_{F814W} \sim 0.064$. This value is quite consistent with the mass-to-light ratio in H band of 0.05 found for the larger starburst region by Marquart et al. (2007). Assuming this constant mass-to-light ratio for all the SSCs,

we derived masses as given in Table 3.

We found a total mass in young clusters in the nuclear region to be $\sim 7.4 \times 10^6 M_{\odot}$. This nuclear region overlaps with region A from Johnson et al. (2000), who derived a total mass between $1.6 - 2.6 \times 10^6 M_{\odot}$ from UV spectra. This large discrepancy might arise from their assumed IMF, which like Chandar et al. (2003) used Salpeter IMF between 1-100 M_{\odot} (see above).

4.4. Dynamical Friction Timescale

4.4.1. Galaxy Density Profile Determination

In addition to the cluster parameters, we require the central density profile of the galaxy to determine the dynamical friction timescales. Following Antonini (2013), we characterize the central starburst region of Henize 2-10 with a simple power-law density profile, $\rho(r) = \rho_0(r/r_0)^{-\gamma}$. There are three parameters we need to specify: the central stellar mass density, ρ_0 , the scale radius

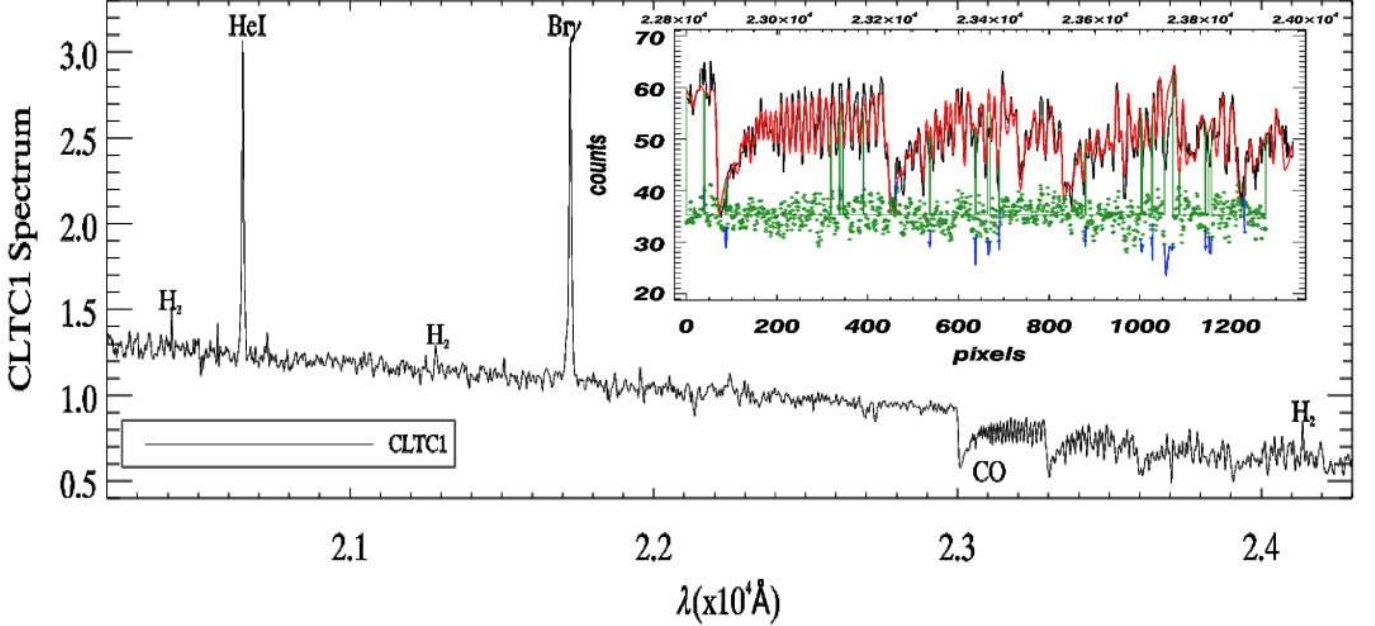


FIG. 7.— The normalized spectra of the brightest SSC (CLTC1) after subtracting off the local background. Labels show emission from Br γ , HeI, and H $_2$ (1-0 S(1) and 1-0 Q(1)), as well as the CO absorption bandheads. The inset plot shows the kinematic fit to the CO absorption bandhead region. The black solid line is the observed spectrum, the solid red line is the best fit kinematic model. The green data points are the data-model residuals; blue lines indicate the regions of the spectrum excluded from the fit

TABLE 4
DYNAMICAL FRICTION QUANTITIES FOR SSCs

SSCs (1)	r_{in} (2) (pc)	r_{lt} (3) (pc)	r_{dis} (4) (pc)	τ_{dyn} (5) $\times 10^8$ (yr)
CLTC1	64.8 ± 1.4	7	6	1.7 ± 0.5
CLTC2	36.9 ± 1.4	5	4	0.8 ± 0.2
CLTC3	20.4 ± 1.4	2	7	0.14 ± 0.04
CLTC4	11.2 ± 1.4	2	3	0.04 ± 0.01
5	86.4 ± 1.4	7	2	34 ± 10
6	77.6 ± 1.4	6	2	24 ± 7
7	114.5 ± 1.4	6	6	22 ± 1
8	130.7 ± 1.4	7	3	11 ± 3
9	74.1 ± 1.4	4	2	16 ± 5
10	70.2 ± 1.4	4	2	7 ± 2
11	55.8 ± 1.4	2	5	24 ± 7

NOTE. — NOTES: Dynamical friction quantities of 11 SSCs in the FOV of NIFS. Column (1): SSCs' labels. Column (2): initial galactocentric position; column (3): limiting tidal radius at the SSCs current position; column (4): distance from the galactic center at which the SSC is disrupted; Column (5): dynamical timescales calculated from Eq. (1) which incorporates this effect of the interaction with the galactic tidal field into the calculation. The numbers in this column assume a density profile with $\gamma=0.5$.

of the bulge, r_0 , and power-law index, γ .

Due to the presence of the central starburst, measuring the central profile of the galaxy is not straightforward. While our SB profile fits did not include the central region, we can extrapolate the expected density from those profiles to determine the central density profile. We are thus assuming the central density is dominated by the extrapolation of the older stellar populations as captured by our two-Sérsic component fit, and not the young starburst which likely contributes only a small fraction of the mass despite dominating the optical luminosity at the center.

To facilitate deprojection of the SB profile to a 3D mass density profile, we create a Multiple Gaussian Expansion (MGE) (Emsellem et al. 1994; Cappellari 2002) model based on the two component SB profile presented in §3. In order to translate this luminosity profile into a mass profile, we use the observed kinematics in the central region ($\sigma = 45 \text{ km s}^{-1}$ Marquart et al. 2007) to constrain the mass-to-light ratio. Specifically, we created a Jeans Axisymmetric Model (Cappellari 2008) to predict the dispersion in the central region based on the MGE model. We fix the mass-to-light ratio of the outer component's Sérsic profile to $M/L_r = 2.5$, while varying that of the inner Sérsic component to match the observed dispersion. The best-fit requires a $M/L \sim 2$ for this inner component. We then fit the deprojected MGE density model to the $\rho(r) = \rho_0(r/r_0)^{-\gamma}$ profile within the central $3''$. The best fit parameters are: $\rho_0 = 78 M_\odot \text{ pc}^{-3}$, $r_0 = 95 \text{ pc}$, and $\gamma = 0.5$.

4.4.2. Cluster Limiting Radii & Dissolution

Now that we have a model for the central potential in the galaxy, we can determine whether each cluster is currently tidally limited and whether the clusters will reach the center without being disrupted by the gravitational field of the galaxy and BH. Specifically, we use Antonini (Eq. 23 of 2013) to calculate each cluster limiting tidal

radius r_{lt} :

$$r_{lt} = \frac{\sigma_K}{\sqrt{2}} \left[4\pi G \rho_0 \left(\frac{r}{r_0} \right)^{-\gamma} \frac{\gamma}{3-\gamma} + \frac{3GM_\bullet}{r^3} \right]^{-1/2} \quad (4)$$

where r is the projected distance between each cluster and the position of the BH, and M_\bullet is the BH's mass. The projected distance of each SSC is listed in the column 2 of Table 4. σ_K is SSC's velocity dispersion which is estimated from the mass and profile estimate listed in the column 2 of Table 1, except for CLTC1 where we use our measurement. We find that in each cluster the limiting radius is larger than the best-fit core radius, but smaller than the tidal radius (we fit all data to a $c = 30$ King model, thus $r_t = 30r_c$ listed in column 3 of Table 4). This means each cluster is already being limited by the gravitational potential of the galaxy, and thus should have a dynamical friction timescale given by equation 1 which incorporates the affects of mass loss as the cluster moves inwards.

The clusters may be disrupted by the external gravitational field before reaching the center of the galaxy; following Antonini (2013) we assume this occurs when the limiting radius is equal to the core radius of each cluster. This galactocentric radius is given in column 4 of Table 4; each cluster should survive until it is within the central 10 pc (and in most cases the central 5 pc). Given that typical NSCs have effective radii of ~ 4 pc (e.g., Côté et al. 2006), each cluster is likely to add at least some of its mass to a forming NSC if their dynamical friction timescales are short enough.

Internal processes could also shorten the lifetimes of these clusters; substantial natal gas or stellar wind mass loss could cause the clusters to dissolve. However, the clusters are already optically visible and thus have likely lost their natal gas. Furthermore, stellar wind mass loss represents $< 30\%$ of the clusters mass within the first 500 Myr of a cluster (Gieles 2010), and thus this effect is unlikely to dissolve these massive clusters. Finally, we expect dissolution from two body relaxation to be very slow; the clusters have relaxation times of $> 5 \times 10^8$ yr; dissolution due to dynamical evolution occurs over many relaxation times (Spitzer 1987; Binney & Tremaine 2008).

4.4.3. Dynamical Friction Timescales

Finally, we calculate the clusters' dynamical friction timescales using Eq. (1) (Eq. 32 of Antonini 2013). These timescales are given in column 5 of Table 4; for the most massive clusters these timescales are $< 10^9$ years. The most massive cluster, CLTC1 has a timescale of just 170 Myr. Thus a nuclear cluster well in excess of $10^6 M_\odot$ is likely to form within a few hundred Myr. The end product will have the appearance of a NSC; the faintest NSCs in $\sim 10^{10} M_\odot$ galaxies typically have NSCs of $10^6 M_\odot$ (Seth et al. 2008). Because the timescale of formation is so short relative to the age of the Universe, the state we are seeing in Henize 2-10 should be rare.

Henize 2-10 thus provides an interesting snapshot of NSC formation in action and constraints on the coevolution of NSCs and BHs. While there have been previous suggestions that massive clusters may provide the seeds for BHs (e.g., Portegies Zwart et al. 2004), if there is any coevolution between the two components in Henize 2-10

it would be due to merger fed mutual growth as modeled by Hopkins & Quataert (2010b,a). Thus while the NSC is forming, the BH may also grow through gas accretion or the accretion of stars (Bromley et al. 2012). However, as we argued in §3.3, it appears likely based on the galaxy's overall mass and early-type nature that a BH was already present in the galaxy, and that the growth of the NSC is occurring after BH formation. This would suggest that the formation of the NSC and BH, at least in this galaxy, is largely uncorrelated.

5. HENIZE 2-10 NUCLEAR SPECTRUM

There are several ways an accreting BH could be detected from our K -band NIFS spectrum: (1) dynamical modeling of the stellar velocity dispersion in the vicinity of BH (e.g., Krajnović et al. 2009), (2) detection of coronal line emission such as Al IX, which requires extreme emission from the region around the accreting BH to excite (e.g., Storchi-Bergmann et al. 2009), or (3) detection of other emission lines, such as Br γ , which might be associated with X-ray radiation from the accreting region.

To determine if the BH may be dynamically detectable from our kinematics observations we first consider the sphere of influence of the BH. The mass of the BH was estimated to be $2 \times 10^6 M_\odot$ by Reines et al. (2011) based on the fundamental plane which provides order of magnitude estimates of BH masses (e.g., Merloni et al. 2003). The dispersion in the inner region of the galaxy outside of the star clusters is $\sigma \sim 45 \text{ km s}^{-1}$. Using this dispersion, the sphere of influence (SOI) is given as $r_{\text{SOI}} = GM_{\text{BH}}/\sigma^2 \sim 4 \text{ pc}$ or $\sim 0''.1$. This is comparable to the PSF FWHM of $0''.15$ and thus it may be possible to see the effect of a BH on the kinematics. We note however that there is considerable uncertainty in the BH mass estimate and therefore in the sphere of influence.

There is no clear detection of a dispersion peak or enhanced rotation in the vicinity of the BH; in fact, the dispersion is lower at the location of the BH than in the surrounding areas (Fig. 2). To better understand the expected signal from the BH, we use our Jeans model for the center of the galaxy derived in §4.4 to simulate our NIFS observations with the addition of a BH with mass between 0 and $10^7 M_\odot$. We find that for a BH of mass $2 \times 10^6 M_\odot$ we would expect an increase in dispersion of $\sim 1.5 \text{ km s}^{-1}$; this is smaller the 1σ random errors on our measurement and thus a BH of this mass cannot be ruled out. We can place a firm upper limit of $\sim 10^7 M_\odot$ on the BH which would increase the dispersion by $\sim 7 \text{ km s}^{-1}$ and thus be clearly detectable at the 3σ level in our data. Another possibility is that the BH is significantly obscured and the stars we are seeing are in the foreground of the BH. If this were the case, the obscuring material would need to be on scales larger than the sphere of influence.

We also searched for Al IX coronal line emission in the vicinity of the BH and did not find a convincing detection. This line has an ionization energy of 285 eV, thus requiring X-ray emission likely only generated by an AGN (e.g., Satyapal et al. 2008). The only other coronal line in our bandpass is the Ca VIII line which falls on top of the CO bandhead region and thus is challenging to detect at weak flux levels. We place a 3σ upper limit

on the Al IX luminosity of $4 \times 10^{-17} \text{ erg s}^{-1} \text{ cm}^{-2}$.

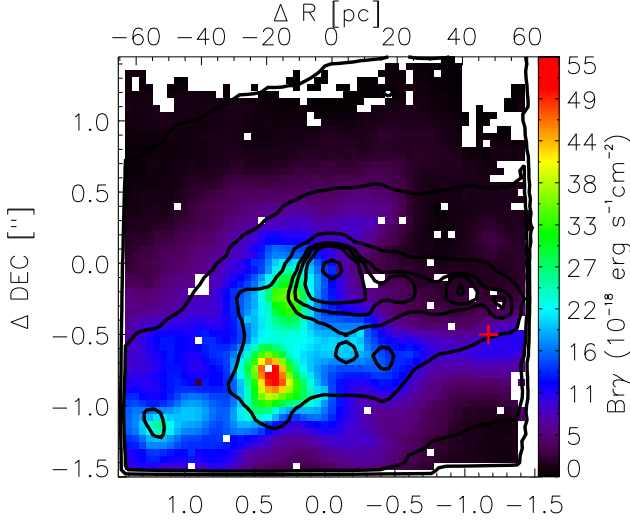


FIG. 8.— $\text{Br}\gamma$ emission of the starburst region in the NIFS $3'' \times 3''$ FOV. Colors and color bar indicate the flux of the $\text{Br}\gamma$ line emission. White areas have $\text{Br}\gamma$ emission with $\text{SNR} < 3$. The red cross represents the position of BH; significant $\text{Br}\gamma$ emission is located at this position. Contours indicate K -band surface brightness of 15.7, 15.9, 16.1, 16.6, and 17.7 $\text{mag}/''^2$. The coordinates are centered on the continuum peak of the brightest cluster, CLTC1.

Fig. 8 shows the $\text{Br}\gamma$ emission map within our NIFS FOV. This map shows a clear enhancement of $\text{Br}\gamma$ emission at the AGN's position (red cross is the BH's suggested location with an astrometric uncertainty of $\sim 0''.1$). To examine this $\text{Br}\gamma$ peak in more detail, we create a nuclear spectrum around this source with a radius of $0.2''$ and sky annulus is about 10% of the total $\text{Br}\gamma$ flux. This spectrum is shown in Fig. 9; the main panel shows the spectrum, while the small upper right panel shows a zoom-in of the dominant emission line, $\text{Br}\gamma$. No broad $\text{Br}\gamma$ emission is seen.

The total $\text{Br}\gamma$ luminosity is $(3.2 \pm 0.3) \times 10^{36} \text{ erg s}^{-1}$. We can compare this luminosity to the X-ray luminosity to evaluate whether the AGN could be the source of the observed $\text{Br}\gamma$ line or not. The best fit power law model for the source gives an X-ray luminosity is $L_{2-10} = 2.7 \times 10^{39} \text{ erg s}^{-1}$ (Reines et al. 2011). This best fit also gives $N_{H,\text{pow}} = 6.3^{+5.5}_{-3.6} \times 10^{22} \text{ cm}^{-2}$ which corresponds to $A_V \sim 14 - 60$. We can convert the X-ray luminosity to an expected $\text{Br}\gamma$ luminosity; Panessa et al. (2006) derives an empirical linear relationship of X-ray to H_α luminosity for a sample of 47 AGNs and 30 QSOs: $\log_{10} L_X = (1.06 \pm 0.04) \log_{10} L_\alpha - (1.15 \pm 0.85)$; it appears that this error bar is misprinted; we recalculated the error on the relation by examining the scatter in the data and found a zeropoint error of 0.85, therefore we assume a relation $\log_{10} L_X = (1.06 \pm 0.04) \log_{10} L_\alpha - (1.15 \pm 0.85)$. We also note that this relation may not hold at low accretion rates or at low masses (e.g., for Henize 2-10).

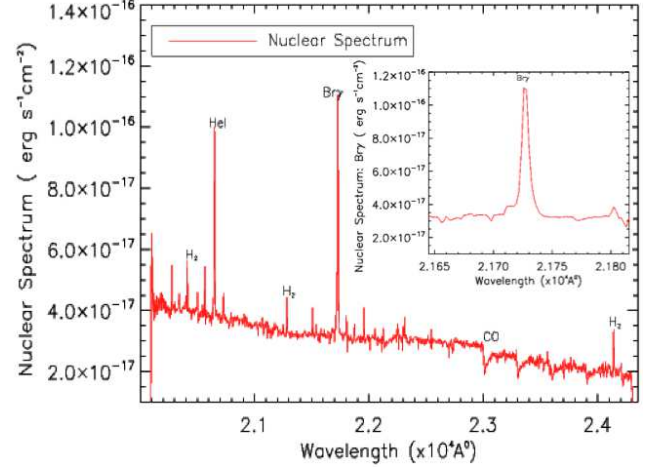


FIG. 9.— NIFS spectrum of AGN within $0.2''$ aperture with detected emission lines of $\text{Br}\gamma$, HeI , and H_2 (1-0 S(1) and 1-0 Q(1)) and CO absorption lines are marked. The smaller panel indicates the significantly detected $\text{Br}\gamma$ emission only.

Proceeding with this caveat, the predicted $L_{H\alpha}$ luminosity ranges from $7.56 \times 10^{38} \text{ erg s}^{-1}$ to $9.38 \times 10^{38} \text{ erg s}^{-1}$. Next, assuming case B recombination and a temperature of $T = 10,000 \text{ K}$, the ratio of $\text{Br}\gamma/H_\alpha$ is 0.01 (Osterbrock 1989). Thus the predicted $\text{Br}\gamma$ luminosity is between $7.56 \times 10^{36} \text{ erg s}^{-1}$ and $9.38 \times 10^{36} \text{ erg s}^{-1}$. The error in this determination is dominated by the error on the conversion between L_X and $L_{H\alpha}$; the conversion from H_α to $\text{Br}\gamma$ is similar over the full range of reasonable temperatures (i.e., 5,000–20,000 K).

We now estimate whether this predicted $\text{Br}\gamma$ luminosity is consistent with the observed luminosity given the extinction values from the X-ray data and observed from line-emission ratios by Cresci et al. (2010). With the observed and the predicted $\text{Br}\gamma$ luminosity above, the ratio $L_{\text{Br}\gamma,\text{pre}}/L_{\text{Br}\gamma,\text{obs}} \sim 2.4 - 3.0$; therefore, assuming the Cardelli et al. (1989) extinction law, the extinction suggested is $A_V \sim 8 - 12$ or corresponding to a hydrogen column of $N_H = 1.5^{+0.75}_{-0.00} \times 10^{22} \text{ cm}^{-2}$ Bohlin et al. (1978). The extinction maps of Cresci et al. (2010) show values between $A_V \sim 2 - 14$; nearest the location of the AGN, the average extinction is approximately $A_V = 10.6$. The hydrogen column also overlaps with the poorly constrained Hydrogen column fit from the X-ray spectrum by Reines et al. (2011) of $N_{H,\text{pow}} = 6.3^{+5.5}_{-3.6} \times 10^{22} \text{ cm}^{-2}$. Thus it is plausible that the $\text{Br}\gamma$ emission we observe is coming from accretion onto the BH.

If the $\text{Br}\gamma$ emission is indeed from the BH, it allows us to measure the velocity of the BH relative to the galaxy as a whole. Fitting the spectrum shown in Fig. 9 (with $r = 0.2''$), the $\text{Br}\gamma$ radial velocity is $(28.3 \pm 1.5) \text{ km s}^{-1}$ redshifted relative to systemic velocity of the galaxy and its velocity dispersion is $(23.7 \pm 0.7) \text{ km s}^{-1}$ taking into account the local instrumental dispersion. We assume the systemic velocity of the galaxy is $\sim 872 \pm 6 \text{ km s}^{-1}$ (Marquart et al. 2007).

6. CONCLUSIONS

We have examined the overall morphology and nuclear regions of Henize 2-10 using ground-based photometric data, adaptive optics Gemini/NIFS data and *HST* data. Our primary findings are:

1. Henize 2-10 is well fit by a two component Sérsic profile. The inner Sérsic profile has $n \sim 0.6$ and $r_{\text{eff}} \sim 6''$ (~ 258 pc), and the outer Sérsic profile has $n \sim 1.8$ and $r_{\text{eff}} \sim 25''$ (~ 1 kpc). The absolute magnitude of Henize 2-10 within 4.3 kpc is $M_g = -19.2 \pm 0.2$, $M_r = -19.8 \pm 0.4$ in g -band and r -band.
2. The total stellar mass of Henize 2-10 within 4.3 kpc is $(10 \pm 3) \times 10^9 M_\odot$ as derived from the r -band, a factor of ~ 3 times higher than previous estimates based on the K -band luminosity.
3. Apart from the inner starburst, Henize 2-10 appears to be typical early-type galaxy. Its outer color $(g - r)_0 = 0.75$ is consistent with an old population. Furthermore, it is non-rotating and dispersion-dominated near the center and has an outer Sérsic index consistent with other early-type galaxies of similar luminosity.
4. We estimate the dynamical mass of the brightest SSC in Henize 2-10 to be $2.3 \pm 0.6 \times 10^6 M_\odot$, higher than previous estimates. We use this mass estimate to derive new masses for 11 clusters at the center of Henize 2-10, assuming a constant M/L for all the clusters.
5. The timescale for dynamical friction is $< 10^9$ years for the SSCs at the center of Henize 2-10. An NSC of mass $> 10^6 M_\odot$ should be formed within a few hundred Myr; this cluster mass would be typical

for galaxies of Henize 2-10's mass. Thus, we are seeing NSC formation in progress in this galaxy, and this formation appears to be independent of the formation of the BH in this system.

6. While there are few examples of $M_\star < \sim 10^{10} M_\odot$ star-forming galaxies with observational evidence for a massive BH (e.g., Greene 2012; Schramm et al. 2013; Reines et al. 2014), the occupation fraction of massive BHs in early-type galaxies of this mass is likely $\sim 90\%$ (Miller et al. 2014). Therefore, it is reasonable that Henize 2-10 hosts a massive BH. Our observations allow us to place a firm upper limit on the BH mass of $M_\bullet < 10^7 M_\odot$. We do not detect coronal emission from the BH, but Br gamma emission consistent with the X-ray emission is detected at the location of the BH.

We would like to thank Maureen Conroy at the SAO/TDC for providing us the Magellan/Megacam data of g -, i -, and r -bands, Micheva Genoveva for generously sharing us with her SB profiles in 5 Bessel-Johnson filters *UBVHK*, and the University of Utah, Physics and Astronomy Department for supporting this work. The authors also thank Fabio Antonini for helpful discussions. Support for Amy E. Reines was provided by NASA through the Einstein Fellowship Program, grant PF1-120086.

REFERENCES

- Agarwal, M., & Milosavljević, M. 2011, *ApJ*, 729, 35
- Antonini, F. 2013, *ApJ*, 763, 62
- . 2014, ArXiv e-prints, arXiv:1402.4865
- Antonini, F., Capuzzo-Dolcetta, R., Mastrobuono-Battisti, A., & Merritt, D. 2012, *ApJ*, 750, 111
- Barth, A. J. 2004, *Coevolution of Black Holes and Galaxies*, 21
- Barth, A. J., Greene, J. E., & Ho, L. C. 2008, *AJ*, 136, 1179
- Bertin, E., & Arnouts, S. 1996, *A&AS*, 117, 393
- Bertin, E., Mellier, Y., Radovich, M., et al. 2002, in *Astronomical Society of the Pacific Conference Series*, Vol. 281, *Astronomical Data Analysis Software and Systems XI*, ed. D. A. Bohlender, D. Durand, & T. H. Handley, 228
- Binney, J., & Tremaine, S. 2008, *Galactic Dynamics: Second Edition* (Princeton University Press)
- Bohlin, R. C., Savage, B. D., & Drake, J. F. 1978, *ApJ*, 224, 132
- Böker, T., Laine, S., van der Marel, R. P., et al. 2002, *AJ*, 123, 1389
- Bromley, B. C., Kenyon, S. J., Geller, M. J., & Brown, W. R. 2012, *ApJ*, 749, L42
- Caldwell, N. 1999, *AJ*, 118, 1230
- Calzetti, D., Kennicutt, R. C., Engelbracht, C. W., et al. 2007, *ApJ*, 666, 870
- Cappellari, M. 2002, *MNRAS*, 333, 400
- . 2008, *MNRAS*, 390, 71
- Cappellari, M., & Copin, Y. 2003, *MNRAS*, 342, 345
- Cappellari, M., & Emsellem, E. 2004, *PASP*, 116, 138
- Cardelli, J. A., Clayton, G. C., & Mathis, J. S. 1989, *ApJ*, 345, 245
- Chandar, R., Leitherer, C., Tremonti, C., & Calzetti, D. 2003, *ApJ*, 586, 939
- Chandrasekhar, S. 1943, *Annals of the New York Academy of Sciences*, 45, 131
- Cid Fernandes, R., González Delgado, R. M., Storch-Bergmann, T., Martins, L. P., & Schmitt, H. 2005, *MNRAS*, 356, 270
- Corbin, M. R., Korista, K. T., & Vacca, W. D. 1993, *AJ*, 105, 1313
- Côté, P., Piatek, S., Ferrarese, L., et al. 2006, *ApJS*, 165, 57
- Cresci, G., Vanzi, L., Sauvage, M., Santangelo, G., & van der Werf, P. 2010, *A&A*, 520, A82
- Desroches, L.-B., & Ho, L. C. 2009, *ApJ*, 690, 267
- Emsellem, E., Monnet, G., & Bacon, R. 1994, *A&A*, 285, 723
- Engelbracht, C. W., Gordon, K. D., Rieke, G. H., et al. 2005, *ApJ*, 628, L29
- Ferrarese, L., Côté, P., Dalla Bontà, E., et al. 2006a, *ApJ*, 644, L21
- Ferrarese, L., Côté, P., Jordán, A., et al. 2006b, *ApJS*, 164, 334
- Fukugita, M., Ichikawa, T., Gunn, J. E., et al. 1996, *AJ*, 111, 1748
- Gallo, E., Treu, T., Marshall, P. J., et al. 2010, *ApJ*, 714, 25
- Gavazzi, G., Donati, A., Cucciati, O., et al. 2005, *A&A*, 430, 411
- Gieles, M. 2010, in *IAU Symposium*, Vol. 266, *IAU Symposium*, ed. R. de Grijs & J. R. D. Lépine, 69–80
- Graham, A. W. 2012, *MNRAS*, 422, 1586
- Greene, J. E. 2012, *Nature Communications*, 3, arXiv:1211.7082
- Greene, J. E., & Ho, L. C. 2007, *ApJ*, 670, 92
- Greene, J. E., Ho, L. C., & Barth, A. J. 2008, *ApJ*, 688, 159
- Hopkins, P. F., & Quataert, E. 2010a, *MNRAS*, 407, 1529
- . 2010b, *MNRAS*, 405, L41
- Jester, S., Schneider, D. P., Richards, G. T., et al. 2009, *MNRAS*, 399, 1839
- Johnson, K. E., Leitherer, C., Vacca, W. D., & Conti, P. S. 2000, *AJ*, 120, 1273
- Just, A., & Jahreiß, H. 2010, *MNRAS*, 402, 461
- Kobulnicky, H. A., Dickey, J. M., Sargent, A. I., Hogg, D. E., & Conti, P. S. 1995, *AJ*, 110, 116
- Kobulnicky, H. A., & Martin, C. L. 2010, *ApJ*, 718, 724
- Koleva, M., de Rijcke, S., Prugniel, P., Zeilinger, W. W., & Michielsen, D. 2009, *MNRAS*, 396, 2133
- Koleva, M., Prugniel, P., de Rijcke, S., & Zeilinger, W. W. 2011, *MNRAS*, 417, 1643
- Kormendy, J., Fisher, D. B., Cornell, M. E., & Bender, R. 2009, *ApJS*, 182, 216
- Kormendy, J., & Ho, L. C. 2013, *ARA&A*, 51, 511

- Krajnović, D., McDermid, R. M., Cappellari, M., & Davies, R. L. 2009, *MNRAS*, 399, 1839
- Krist, J. E., Hook, R. N., & Stoeck, F. 2011, in *Society of Photo-Optical Instrumentation Engineers (SPIE) Conference Series*, Vol. 8127, *Society of Photo-Optical Instrumentation Engineers (SPIE) Conference Series*
- Kroupa, P. 2001, *MNRAS*, 322, 231
- Larsen, S. S. 1999, *A&AS*, 139, 393
- . 2001, *AJ*, 122, 1782
- Larsen, S. S., Brodie, J. P., Sarajedini, A., & Huchra, J. P. 2002, *AJ*, 124, 2615
- Leigh, N., Böker, T., & Knigge, C. 2012, *MNRAS*, 424, 2130
- Leitherer, C., Schaerer, D., Goldader, J. D., et al. 1999, *ApJS*, 123, 3
- Lotz, J. M., Telford, R., Ferguson, H. C., et al. 2001, *ApJ*, 552, 572
- Marquart, T., Fathi, K., Östlin, G., et al. 2007, *A&A*, 474, L9
- McConnell, N. J., & Ma, C.-P. 2013, *ApJ*, 764, 184
- McCady, N., & Graham, J. R. 2007, *ApJ*, 663, 844
- Melbourne, J., Williams, B. F., Dalcanton, J. J., et al. 2012, *ApJ*, 748, 47
- Méndez, D. I., Esteban, C., Filipović, M. D., et al. 1999, *A&A*, 349, 801
- Merloni, A., Heinz, S., & di Matteo, T. 2003, *MNRAS*, 345, 1057
- Merritt, D., Piatek, S., Portegies Zwart, S., & Hensendorff, M. 2004, *ApJ*, 608, L25
- Micheva, G., Östlin, G., Zackrisson, E., et al. 2013, *A&A*, 556, A10
- Miller, B. P., Gallo, E., Greene, J. E., et al. 2014, *ArXiv e-prints*, arXiv:1403.4246
- Milosavljević, M. 2004, *ApJ*, 605, L13
- Noeske, K. G., Papaderos, P., Cairós, L. M., & Fricke, K. J. 2003, *A&A*, 410, 481
- Osterbrock, D. E. 1989, *Astrophysics of gaseous nebulae and active galactic nuclei*
- Ott, J., Walter, F., & Brinks, E. 2005a, *MNRAS*, 358, 1423
- . 2005b, *MNRAS*, 358, 1453
- Panessa, F., Bassani, L., Cappi, M., et al. 2006, *A&A*, 455, 173
- Peterson, C. J., & King, I. R. 1975, *AJ*, 80, 427
- Portegies Zwart, S. F., Baumgardt, H., Hut, P., Makino, J., & McMillan, S. L. W. 2004, *Nature*, 428, 724
- Reines, A. E., & Deller, A. T. 2012, *ApJ*, 750, L24
- Reines, A. E., Greene, J. E., & Geha, M. 2013, *ApJ*, 775, 116
- Reines, A. E., Plotkin, R. M., Russell, T. D., et al. 2014, *ApJ*, 787, L30
- Reines, A. E., Sivakoff, G. R., Johnson, K. E., & Brogan, C. L. 2011, *Nature*, 470, 66
- Santangelo, G., Testi, L., Gregorini, L., et al. 2009, *A&A*, 501, 495
- Satyapal, S., Vega, D., Dudik, R. P., Abel, N. P., & Heckman, T. 2008, *ApJ*, 677, 926
- Schlaafly, E. F., & Finkbeiner, D. P. 2011, *ApJ*, 737, 103
- Schramm, M., Silverman, J. D., Greene, J. E., et al. 2013, *ApJ*, 773, 150
- Scott, N., Graham, A. W., & Schombert, J. 2013, *ApJ*, 768, 76
- Seth, A. C., Blum, R. D., Bastian, N., Caldwell, N., & Debattista, V. P. 2008, *ApJ*, 687, 997
- Seth, A. C., Cappellari, M., Neumayer, N., et al. 2010, *ApJ*, 714, 713
- Skrutskie, M. F., Cutri, R. M., Stiening, R., et al. 2006, *AJ*, 131, 1163
- Smith, J. A., Tucker, D. L., Kent, S., et al. 2002, *AJ*, 123, 2121
- Spitzer, L. 1987, *Dynamical evolution of globular clusters*
- Storchi-Bergmann, T., McGregor, P. J., Riffel, R. A., et al. 2009, *MNRAS*, 394, 1148
- Strader, J., Smith, G. H., Larsen, S., Brodie, J. P., & Huchra, J. P. 2009, *AJ*, 138, 547
- Toloba, E., Guhathakurta, P., van de Ven, G., et al. 2014, *ApJ*, 783, 120
- Tremaine, S. D., Ostriker, J. P., & Spitzer, Jr., L. 1975, *ApJ*, 196, 407
- Vacca, W. D., Johnson, K. E., & Conti, P. S. 2002, *AJ*, 123, 772
- Verolme, E. K., Cappellari, M., Copin, Y., et al. 2002, *MNRAS*, 335, 517
- Volonteri, M. 2010, *A&A Rev.*, 18, 279
- Wallace, L., & Hinkle, K. 1996, *ApJS*, 107, 312
- Wehner, E. H., & Harris, W. E. 2006, *ApJ*, 644, L17
- Worthey, G. 2004, *AJ*, 128, 2826
- Zibetti, S., Charlot, S., & Rix, H.-W. 2009, *MNRAS*, 400, 1181